Supplementary Information (SI) for Nanoscale.

Supplementary Information

Impact of processing atmosphere on nanoscale properties of highly efficient $Cs_{0.05}MA_{0.05}FA_{0.9}PbI_3$ perovskite solar cells

Muhammad Uzair Farooq,[1] Sevan Gharabeiki,[1] Ding Yong,[2] Joana Ferreira Machado,[3] Jean-Nicolas Audinot,[4] Tom Wirtz,[4] Mohammad Khaja Nazeeruddin,[2] Susanne Sienbentritt,[1] and Alex Redinger[1]

[1] *Department of Physics and Materials Science, University of Luxembourg, Luxembourg City L-1511, Luxembourg*

[2] *Group for Molecular Engineering of Functional Material, Institute of Chemical Sciences and Engineering, École Polytechnique Fédérale de Lausanne, Sion CH-1951, Switzerland*

[3] *Department of Physics and Materials Science, University of Luxembourg, Luxembourg City L-1511, Luxembourg*

[4] *Advanced Instrumentation for Nano-Analytics (AINA), Luxembourg Institute of Science and Technology (LIST), L-4362 Esch-sur-Alzette, Luxembourg*

(*Electronic mail: alex.redinger@uni.lu)

(Dated: 18 February 2025)

A. Materials

The materials used in the experiments included: lead(II) iodide (PbI_2; 99.99%, TCI), phenethylammonium iodide (PEAI; 99%, Greatcell Solar), tin(II) chloride dihydrate ($SnCl_2 \cdot 2H_2O$; 98%, Acros), titanium(IV) chloride ($TiCl_4$; 99%, Sigma-Aldrich), hydrochloric acid (HCl; 37 wt% in H_2O, Sigma-Aldrich), methylammonium chloride (MACl, 99.99%, Greatcell Solar), formamidinium iodide (FAI; 99.99%, Greatcell Solar), methylammonium iodide (MAI, 99.99%, Greatcell Solar), N,N-dimethylformamide (DMF; 99.8%, Sigma-Aldrich), dimethyl sulfoxide (DMSO; 99.9%, Sigma-Aldrich), 2-propanol (99.5%, Sigma-Aldrich), chlorobenzene (99.8%, Sigma-Aldrich), Spiro-OMeTAD (Borun Tech.), 4-tert-butylpyridine (tBP; Sigma-Aldrich), bis(trifluoromethane)sulfonimide lithium salt (Li-TFSI; 99.95%, Sigma-Aldrich), FK209 Co(III) TFSI salt (Sigma-Aldrich), and acetonitrile (ACN; 99.8%, Sigma-Aldrich).

B. AFM/KPFM and GB analysis

As shown in Figure 1, a mask was extracted from the KPFM image (air-annealed case) to identify regions with secondary work functions. The mask was then overlayed with the amplitude signal (error signal of the topography) image, to locate the areas corresponding to these secondary work functions. The analysis clearly shows that the secondary work functions are specific to individual grains and arise from different facets. The corresponding higher workfunctions are PbI_2 grains.

Figure 2 shows how the band bending (BB) analysis was performed for the grain boundaries (GBs). We took the average of the work functions of the two facets (Θ_G), which was then subtracted from the GB work function (Θ_{GB}), that is, ($\Theta_{GB} - \Theta_G = \text{BB}$). As seen on the right-hand side of Figure 2, a negative value would indicate a downward BB and vice versa for a positive value. Any BB value less than 10 meV was taken as a neutral GB, as this is the limitation of the KPFM measurements.

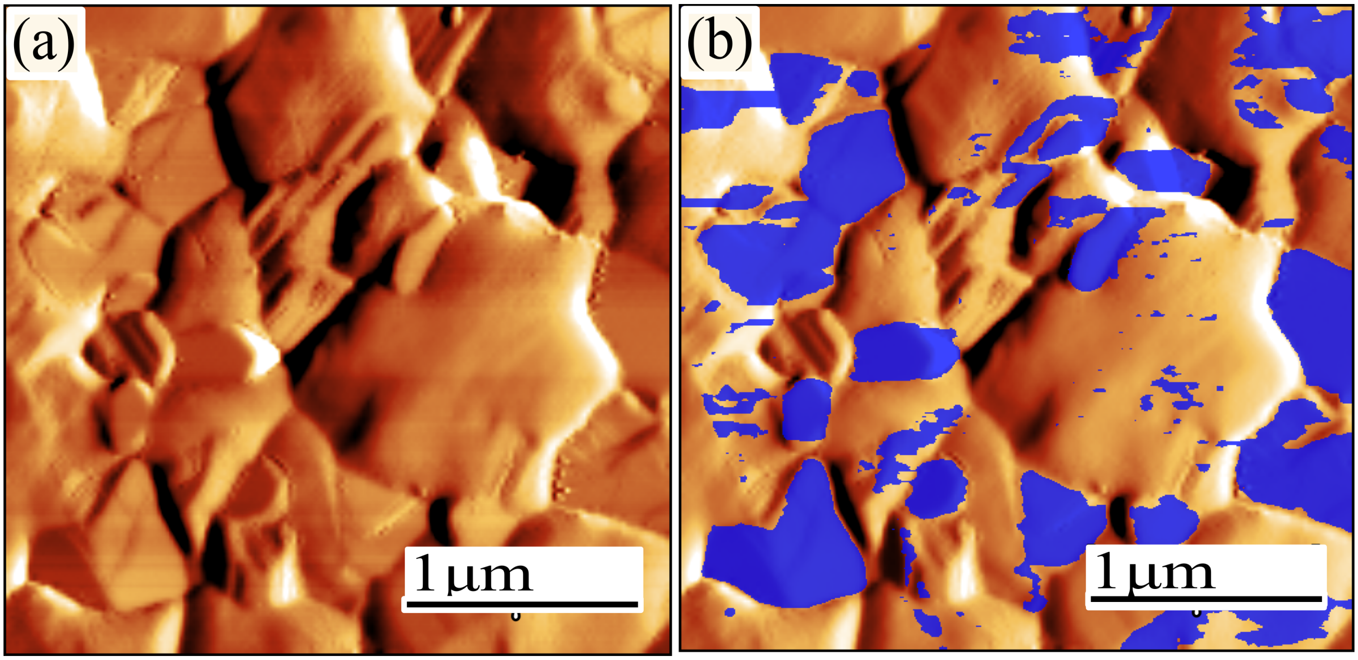

FIG. 1. The blue mask represents the existence of secondary work functions in the topography images (a) Amplitude change map from topography signal (b) Grains covered with blue mask show the secondary workfunction

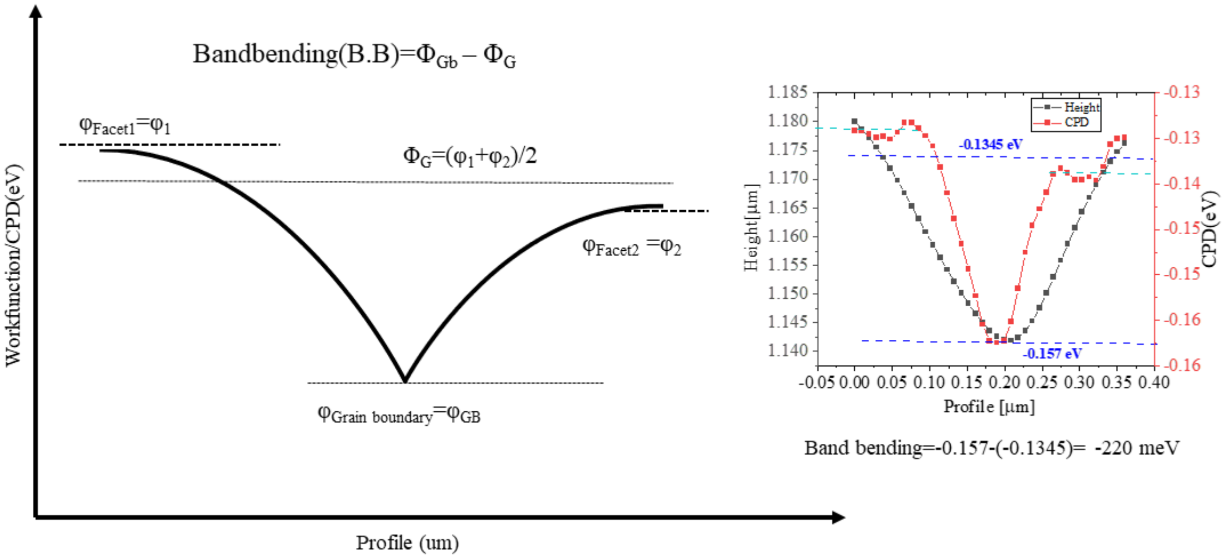

FIG. 2. Left side of the figure explains how the B.B analysis was done on the GBs, right side presents an example from the analysis with a downward BB of 22 meV

C. HIM-SIMS analysis

Figure 3 an overview of the HIM-SIMS mapping for all three cases. The data clearly show that a reduction in the FA^+ ions directly results in an increase in the Pb^+ and I^- ions, indicating that PbI_2 as present on the surface for all three cases.

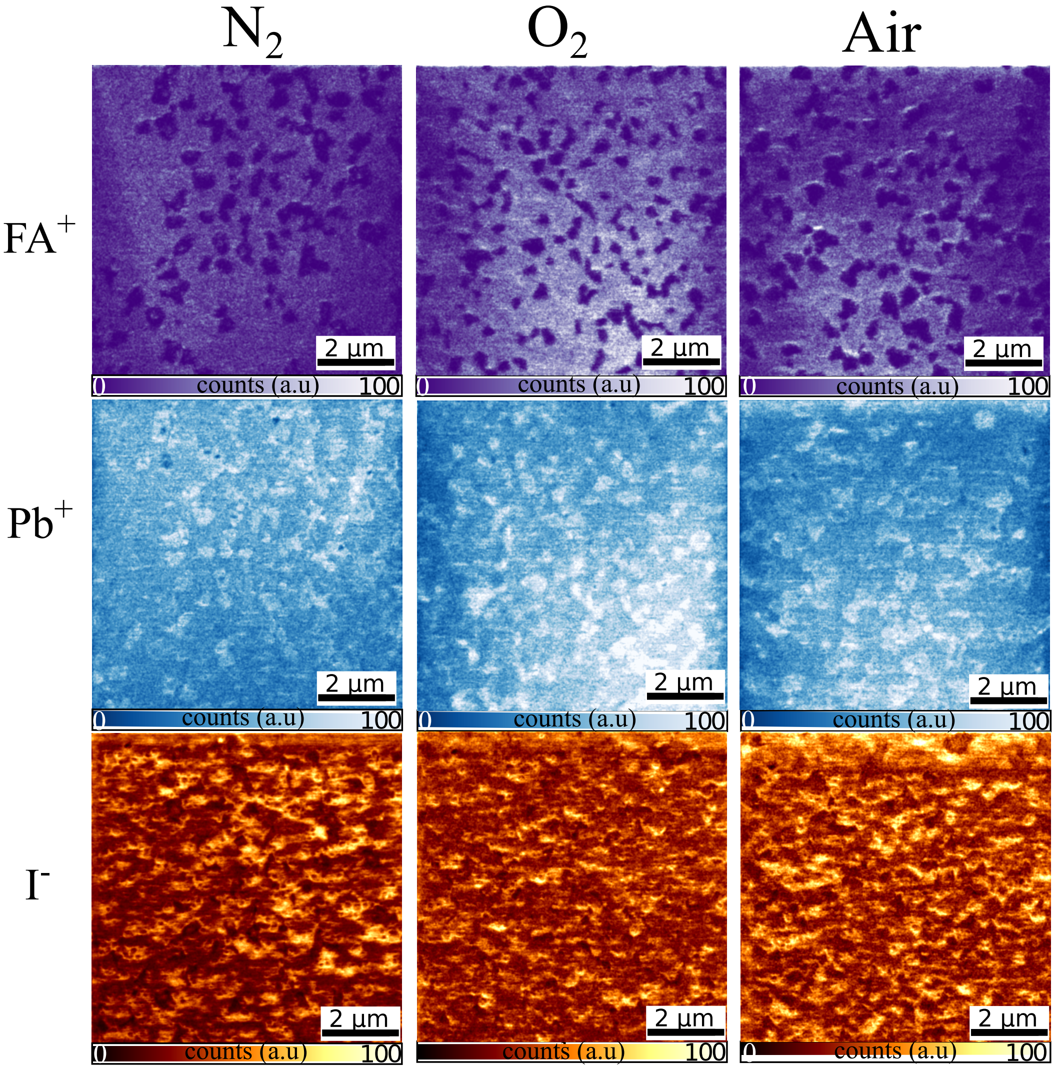

FIG. 3. Elemental composition for all samples, acquired with HIM-SIMS. The purple images represent the elemental distribution for FA^+ ions, blue for Pb^+ ions, and brown for I^-.

Figure 4 shows the elemental composition of the sample annealed in N_2 atmosphere also including the Cs^+ ions. It can be seen that Cs^+ follows the same trend as FA^+, with both showing a reduction in concentration. However, at the same locations, there is an increase in Pb^+ and I^-. Furthermore, this trend is consistent for all three cases.

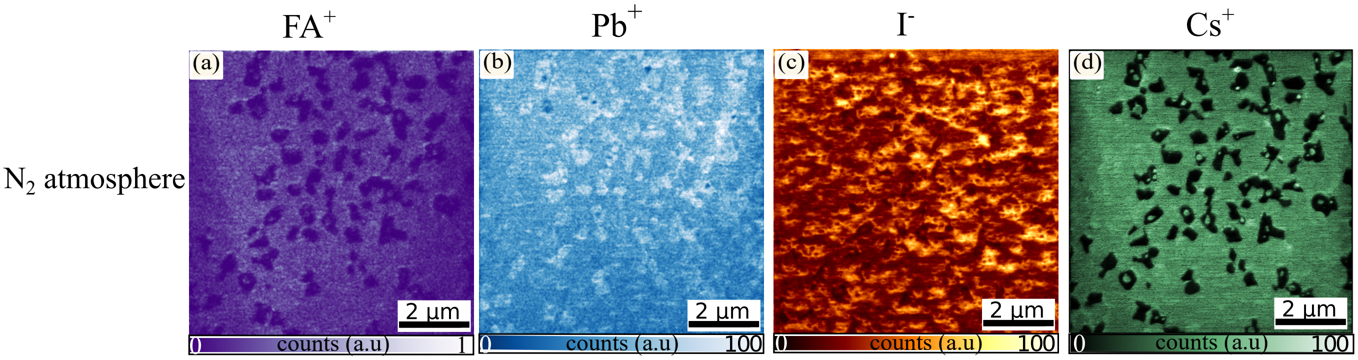

FIG. 4. Elemental composition for N_2 annealed case, including the Cs^+ ions. (a) FA^+ ions, (b) Pb^+ ions, (c) I^- ions, and (d) Cs^+ ions

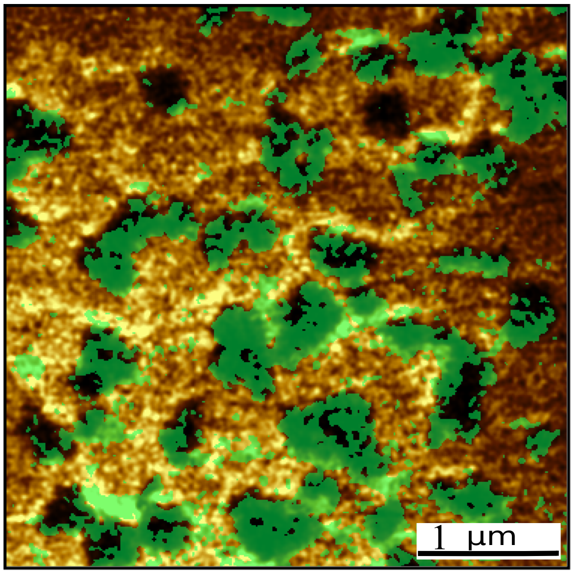

FIG. 5. A mask (green) was extracted from the HIM-SIMS image (Air annealed case) of higher values of Pb^+ and overlaid on the FA^+ image. It can be seen that the excess amount of Pb^+ is correlated to the depletion of FA^+.

D. PL/TRPL

The measured TRPL decay time is always a convolution of surface and bulk lifetimes, i.e.

$$\tau_{eff} = 1/\tau_b + 1/\tau_s \tag{1}$$

The surface-related term is given by:

$$\tau_S = \frac{d}{S_{n,p}} + \frac{4}{D} \cdot \left(\frac{d}{\pi}\right)^2 \tag{2}$$

Consequently, the measured decay times in TRPL, which are denoted here as τ_{eff} are a direct function of the absorber thickness (500 nm) and the diffusion coefficient D, which is assumed to be in the order of 0.5 cm²/s.[1] The following graph shows the evolution of τ_S as a function of the surface recombination velocity S$_{n,p}$

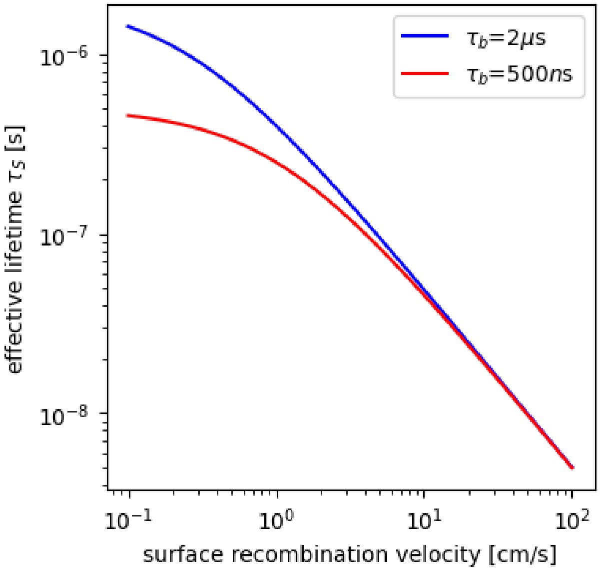

FIG. 6. effective lifetime τ_S as a function of surface recombination velocity for two different bulk lifetimes

Consequently, any variation in the S$_{n,p}$ will directly influence the effective carrier lifetime, particularly in the regime where the velocity is lower than 10 cm/s. As we measure decay times on the order of microseconds for N$_2$-annealed samples, the S$_{n,p}$ must be below 1 cm/s. This conclusion is valid for absorber layers. However, for absorbers covered with an extraction layer or in complete devices, accurate decay time measurements require extensive modeling and cannot be directly interpreted as explained by *Kruckemeier et al.*[2].

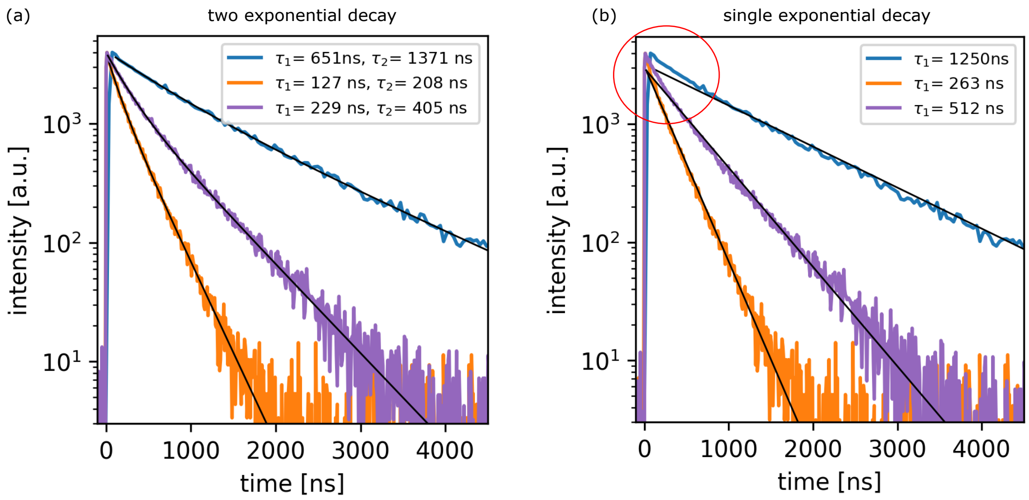

FIG. 7. (a) Background subtracted TRPL spectra fitted with a bi-exponential decay(equation 1) (a) TRPL spectra fitted with a low exponent decay

$$\ln[y(t)] = \ln\left[y_0 + \left(N_1 e^{-\frac{x}{\tau_1}} + N_2 e^{-\frac{x}{\tau_2}}\right)\right] \tag{3}$$

The derivation of the equation originates from[3]. It yields an analytic expression that relates the external photoluminescence quantum yield $Q_{\mathrm{e}}^{\mathrm{lum}}$ to the Schockley-Read-Hall (SRH) lifetime τ, the equilibrium charge carrier concentration p_0, the escape probability p_e and the parasitic absorption p_a. The derivation does not include Auger recombination. The long decay values presented in the main manuscript are input values for the SRH lifetime values. As discussed in[3], $Q_{\mathrm{e}}^{\mathrm{lum}}$ can be expressed as follows:

$$Q_{\mathrm{e}}^{\mathrm{lum}} = \frac{p_{\mathrm{e}} k_{\mathrm{rad}}\, n\,(n + p_0)}{\frac{n}{\tau} + [(1 - p_{\mathrm{r}})\, k_{\mathrm{rad}}\, n(n + p_0)]} \tag{4}$$

The electron concentration in the absorber is defined as n=n_0+Δn whereas the hole concentration is given by p=p_0+Δp, with n_0=N$_D$ and p_0=N$_A$, the ionized donor and acceptor concentration. Δn and Δp are the carrier densities generated during illumination. As a consequence Δn=Δp in all cases. Assuming low injection conditions and a p-type semiconductor $n_0 << \Delta n$, the total electron concentration can be approximated by n$\approx \Delta n$ and the the hole concentration p=n+p$_0$, with $p_0 = N_{\mathrm{A}}$.

Under steady-state and open-circuit voltage conditions, the external generation rate must be equal to the total recombination rate. This leads to the following expression:

$$G_{\mathrm{ext}} = \frac{f}{d} = p_{\mathrm{e}} k_{\mathrm{rad}} n^2 + \frac{n}{\tau} \tag{5}$$

The first term on the right side of the equation arises from radiative recombination ($\propto n^2$), whereas the second term assumes dominant Schockley-Read-Hall recombination (SRH-recombination $\propto n$). The generation rate (G_{ext}) equals the photon flux density f divided by the film thickness d. Solving equation 5 for n and introducing it into equation 4 allows us to express $Q_{\mathrm{e}}^{\mathrm{lum}}$ with the generation rate of charge carriers, which can be measured directly with a power meter. The final expression reads:

$$Q_{\mathrm{e}}^{\mathrm{lum}} = \frac{2\,k_{\mathrm{rad}}\,p_{\mathrm{e}}\,\tau\,(p_0 + G_{\mathrm{ext}}\,\tau)}{1 + (k_{\mathrm{rad}}\,(p_a + p_e)\,\tau\,(p_0 + 2\,G_{\mathrm{ext}}\,\tau) + \tau\sqrt{4\,G_{\mathrm{ext}}\,k_{\mathrm{rad}}\,(p_a + p_e) + \frac{(1 + k_{\mathrm{rad}}\,p_0\,(p_a + p_e)\,\tau)^2}{\tau^2}}} \tag{6}$$

For the case presented in the main paper, the following parameters were used:

Parameter	value	unit
k_{rad}	3E-11	$\mathrm{cm^3 s^{-1}}$
pe	0.05	
pa	0.1	
G_{ext}	4E21	$\mathrm{cm^{-3}\ s^{-1}}$

Figure 9 presents the TRPL spectra fitted with both bi-exponential (a) and single-exponential (b) decay models. In Figure 9 (b) the high injection region is marked with a red circle. A single exponential model does not give an adequate fit in the high region, whereas, a bi-exponential model offers a more accurate fitting of the spectra.

The measured TRPL decay curves were first plotted on a semi-logarithmic scale. Next, the TRPL spectra were fitted using a biexponential decay function as given by 3.

The estimation of the doping of the absorbers are based on a relationship between the carrier lifetime and the photoluminescence quantum yield derived in detail in reference[3]. The reader is referred to this paper for the derivation of the formula. The final equation is

$$Q_{\mathrm{elum}} = \frac{2k_{\mathrm{rad}}p_e\tau\,(p_0 + (G_{\mathrm{ext}}\tau))}{1 + (k_{\mathrm{rad}}(p_a + p_e)\tau\,(p_0 + (2G_{\mathrm{ext}}\tau))) + \tau\sqrt{4G_{\mathrm{ext}}k_{\mathrm{rad}}(p_a + p_e) + \frac{(1 + (k_{\mathrm{rad}}p_0(p_a + p_e)\tau))^2}{\tau^2}}} \tag{7}$$

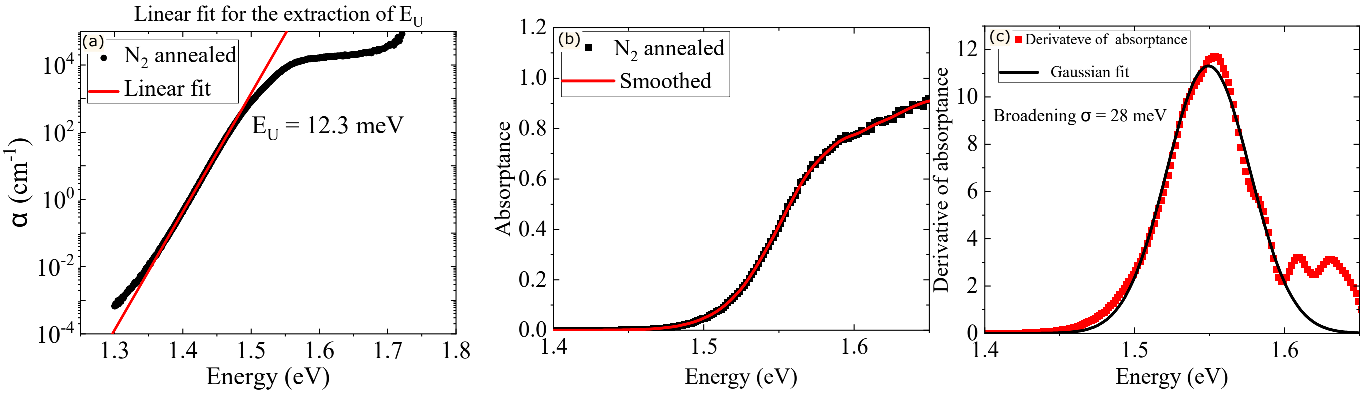

FIG. 8. (a) Linear fit for the extraction of Urbach Energy (E_U) for N_2 annealed case(b) Smoothed absorptance curve (c) I^- ions, and (d) Derivate of the smoothed absorptance curve

The equilibrium charge carrier concentration is given as p_0, $G_{\text{ext}}=\phi/d$ with ϕ the absorbed photon flux and d the thickness of the absorber layer. k_{rad} denoted the radiative recombination coefficient, p_{e} denotes parasitic emission and p_{a} absorption. In equation 7 τ equals to $\tau_n+\tau_p$ for high injection conditions and $\tau=\tau_n$ for low injection conditions. In the main manuscript, where the transients were fitted with a bi-exponential decay curve, we used the long decay time as a measure for τ. This is adequate for the oxygen and air cases, which showed doping densities in the order of 10^{16} 1/cm^3. For the N_2 was not clear whether low or high injection conditions apply. However, as clearly visible in the Figure 3(d) of the main manuscript, at very low doping densities, the method is in any case not very accurate.

For the plot in Figure 3(d) the following parameters were used: $k_{rad} = 3 \cdot 10^{-11}$ cm^3/s, p_e=0.05, $p_a = 0.1$, $G_{ext} = 4 \cdot 10^{21}$ 1/(cm$^3 s$)

E. JV-curves

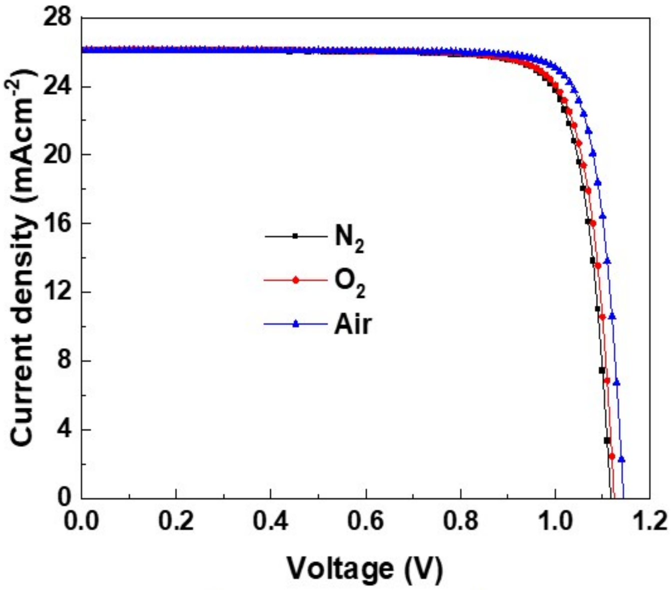

Samples	J_{sc} (mAcm^{-2})	V_{oc} (V)	FF (%)	PCE (%)
N_2	26.08	1.117	82.3	24.00
O_2	26.14	1.125	82.8	24.35
Air	26.08	1.144	84.1	25.12

FIG. 9. JV-curves for all three samples, black scattered line for N_2, red for O_2 and blue for air annealed case

This subsection shows the JV curves for the three cases (Figure 9). The Jsc is similar for all cases. However, the PCE is ultimately determined by the Voc, which is highest for the air-annealed case.

F. SCAPS simulations

The total number of bulk defects (N_t) was chosen such that the lifetime is in agreement with the values acquired from the TRPL results. The capture cross section for electrons and holes at the spiro/perovskite interface was simulated between $1 \cdot 10^{-17}$ cm² and $2 \cdot 10^{-17}$ cm², which changed the surface recombination velocities from 1 cm/s to 2 cm/s, assuming a N_t=$1 \cdot 10^{10}$ 1/cm².

Parameters	SnO_2	CsMAFAPI (Air/N_2)	Spiro-OMeTAD
Thickness(nm)	20	500	20
Bandgap (eV)	3.5	1.54 (via PL)	2.9
e^- affinity(eV)	3.9	3.9[4]	2.2
Permittivity	9.0	22	3.0
CB Effective D.O.S(cm^{-3})	2.2e17	3e18	2.2e18
VB Effective D.O.S (cm^{-3})	2.2e17	3e18	2.2e18
e^- thermal velocity($cm.s^{-1}$)	1e7	1e7	1e7
h^+ thermal velocity($cm.s^{-1}$)	1e7	1e7	1e7
Mobility of e^-($cm^2.v^{-1}s^{-1}$)	2e1	1e1	1e-4
Mobility of h^+($cm^2.v^{-1}s^{-1}$)	1e1	1e1	1e-4
Shallow uniform donor density ND(cm^{-3})	1.8e17	1.3e12	0
Shallow uniform acceptor density NA(cm^{-3})	0	1.3e12	1.3e18

TABLE I. The basic parameters for SCAPS simulations[5].

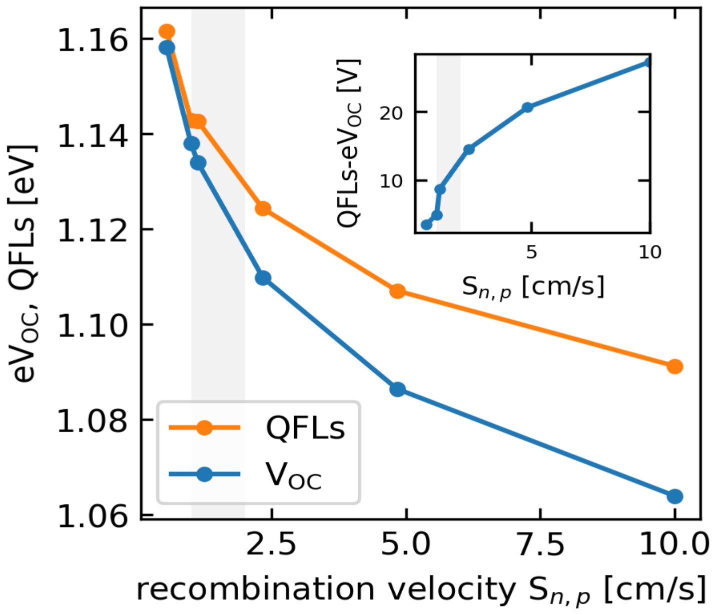

FIG. 10. The graph shows the dependence of Voc (blue) and QFLs (orange) as a function of increasing $S_{\mathrm{n,p}}$. The Inset shows the difference between QFLs and Voc with increasing Surface recombination velocity

Figure 10 shows the dependence of Voc and QFLs with increasing $S_{\mathrm{n,p}}$. As expected, the QFLs values drop with an increase in defects on the surface. However,it is also evident in the plot that the V_{OC} is affected stronger by increasing $S_{\mathrm{n,p}}$. The inset shows the difference of the QFLs and V_{OC} with increasing $S_{\mathrm{n,p}}$, emphasizing that the difference becomes more pronounced at higher $S_{\mathrm{n,p}}$ values. This directly supports our conclusion that the V_{OC} drop in N_2 annealed case is attributed to the poor interface between N_2 annealed perovskite and spiro.

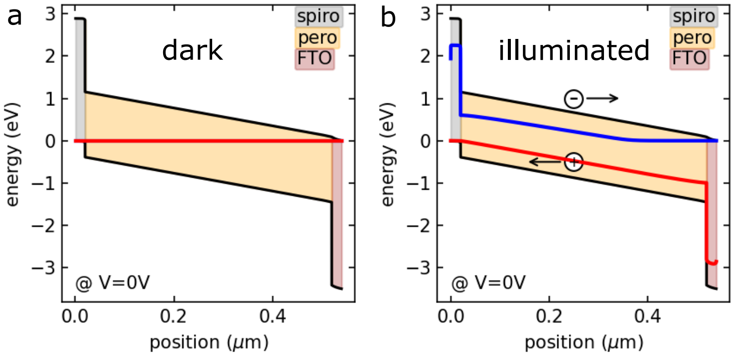

FIG. 11. band diagrams for the device, simulated in SCAPS (a) Equilibrium (dark conditions) (b) Under illumination.

REFERENCES

[1] F. Staub, H. Hempel, J.-C. Hebig, J. Mock, U. W. Paetzold, U. Rau, T. Unold, and T. Kirchartz, "Beyond bulk lifetimes: Insights into lead halide perovskite films from time-resolved photoluminescence," Physical Review Applied **6**, 044017 (2016).

[2] L. Krückemeier, B. Krogmeier, Z. Liu, U. Rau, and T. Kirchartz, "Understanding transient photoluminescence in halide perovskite layer stacks and solar cells," arXiv preprint arXiv:2102.08730 (2021).

[3] T. Kirchartz, J. A. Márquez, M. Stolterfoht, and T. Unold, "Photoluminescence-based characterization of halide perovskites for photovoltaics," Advanced energy materials **10**, 1904134 (2020).

[4] S. Prathapani, P. Bhargava, and S. Mallick, "Electronic band structure and carrier concentration of formamidinium–cesium mixed cation lead mixed halide hybrid perovskites," Applied Physics Letters **112** (2018).

[5] S. Karthick, S. Velumani, and J. Bouclé, "Experimental and scaps simulated formamidinium perovskite solar cells: A comparison of device performance," Solar Energy **205**, 349–357 (2020).